ADVANCED MATERIALS
www.advmat.de

Infrared In-Sensor Computing Based on Flexible Photothermoelectric Tellurium Nanomesh Arrays

Jiachi Liao, He Shao, Yuxuan Zhang, Yan Yan, Ji Zeng, Changyong Lan, Boxiang Gao, Dong Chen, Quan Quan, Pengshan Xie, You Meng, and Johnny C. Ho**

The inherent limitations of traditional von Neumann architectures hinder the rapid development of internet of things technologies. Beyond conventional, complementary metal-oxide-semiconductor technologies, imaging sensors integrated with near- or in-sensor computing architectures emerge as a promising solution. In this study, the multi-scale van der Waals (vdWs) interactions in 1D tellurium (Te) atomic chains are explored, leading to the deposition of a photothermoelectric (PTE) Te nanomesh on a polymeric polyimide substrate. The self-welding process enables the lateral vapor growth of a well-connected Te nanomesh with robust electrical and mechanical properties, including a PTE responsivity of ≈120 V W^{-1} in the infrared light regime. Leveraging the PTE operation, the thermal-coupled bi-directional photoresponse is investigated to demonstrate a proof-of-principle in-sensor convolutional network for edge computing. This work presents a scalable approach for assembling functional vdWs Te nanomesh and highlights its potential applications in PTE image sensing and convolutional processing.

1. Introduction

With the rapid advancement of internet of things technologies, imaging sensors integrated with in-sensor computing have emerged as a promising solution for processing real-time data while addressing the inherent limitations of traditional von Neumann architectures.[1–3] A key aspect of in-sensor computing is its ability to perform convolution operations, which are fundamental for refining image features, such as edge detection. This function is particularly critical for real-time visual processing applications, including object recognition, autonomous navigation, and industrial inspection, where rapid and efficient feature extraction is essential. However, existing image sensing and processing systems face significant performance challenges in low-light or dark environments.[4,5] Conventional imaging sensors based on complementary metal–oxide–semiconductor technologies primarily rely on visible light detection, making them susceptible to ambient light and intensity variations.[6,7] This dependency limits their functionality in poorly lit conditions and reduces their reliability across diverse applications.[8] To overcome these limitations, the development of infrared-sensitive image sensors has gained attention as a transformative approach.[9] Infrared detection offers robust performance in low-visibility scenarios, enhancing the adaptability and resilience of imaging systems.[10,11] These capabilities are particularly valuable for object recognition, feature extraction, and dynamic computing tasks.

Current infrared sensing devices predominantly rely on their constituent materials' intrinsic infrared absorption properties, such as 2D materials with narrow bandgaps, which are widely used to construct heterostructures for infrared detection.[12] However, the reliance on a limited selection of materials with suitable bandgap properties significantly constrains the adaptability and scalability of these devices.[13,14] Moreover, the fabrication of low-dimensional materials often requires complex synthesis methods, demanding precise environmental controls to ensure reproducibility and performance stability.[15,16] Scalable fabrication techniques typically involve high-temperature processing and post-annealing at temperatures exceeding 500 °C to achieve material crystallinity, which restricts their feasibility for mass production and limits their application on temperature-sensitive

J. Liao, H. Shao, Y. Zhang, Y. Yan, B. Gao, D. Chen, Q. Quan, P. Xie, J. C. Ho
Department of Materials Science and Engineering
City University of Hong Kong
Kowloon, Hong Kong SAR 999077, China
E-mail: johnnyho@cityu.edu.hk

J. Zeng, C. Lan
State Key Laboratory of Electronic Thin Films and Integrated Devices
School of Optoelectronic Science and Engineering
University of Electronic Science and Technology of China
Chengdu 610054, China

Y. Meng
Changsha Semiconductor Technology and Application Innovation Research Institute
College of Semiconductors (College of Integrated Circuits)
Hunan University
Changsha 410082, China
E-mail: youmeng@hnu.edu.cn

J. C. Ho
Institute for Materials Chemistry and Engineering
Kyushu University
Fukuoka 816 8580, Japan

J. C. Ho
State Key Laboratory of Terahertz and Millimeter Waves
City University of Hong Kong
Kowloon, Hong Kong SAR 999077, China

The ORCID identification number(s) for the author(s) of this article can be found under https://doi.org/10.1002/adma.202419653

DOI: 10.1002/adma.202419653

substrates, such as polymeric substrates.[17] Furthermore, the performance of these devices is susceptible to factors, such as material growth conditions, interfacial quality, layer thickness, and environmental parameters.[18] These limitations complicate compatibility with standard integrated circuit (IC) manufacturing processes and present substantial challenges for large-scale deployment.

To address the demands of large-area integrated in-sensor computing, scalable growth strategies for low-dimensional materials are essential. In this work, a multi-scale van der Waals (vdWs) growth method was employed to achieve low-temperature deposition of elemental tellurium (Te) nanomesh on various substrates, including flexible polymeric substrates. The resulting Te nanomesh photodetectors exhibit photothermoelectric (PTE) properties, combining excellent compatibility with polymeric substrates and a bandgap-independent photoresponse. Furthermore, the thermal coupling effect between polymeric substrates and PTE films enhances wide-band detection capabilities and enables location-dependent photoresponse. The high-symmetry bidirectional photoresponse of the Te nanomesh array supports the construction of convolutional operators for diverse feature extraction, effectively capturing edges, textures, and spatial patterns. This integrated sensing-computation framework significantly improves robustness and precision in image recognition and processing, offering a novel and efficient solution for advanced edge computing architectures (**Figure 1**a,b).

2. Results and Discussion

2.1. Atmosphere Pressure Growth and Self-Welding Process

The elemental Te crystal consists of helical chains of bonded atoms arranged in a hexagonal array, as illustrated in Figure 1c,d. In addition, the crystal exhibits enantiomeric forms with opposite chiral helices: the right-handed helix belongs to the space groups $P3_121$ and the left-handed helix belongs to the space group $P3_221$, each with distinct rotational properties (Figure S1, Supporting Information). The calculated band structure of Te reveals a band gap of ≈0.34 eV at the high-symmetry point H in the Brillouin zone (Figure S2, Supporting Information). In this study, the Te nanomesh is prepared using a vapor deposition method under atmospheric pressure without the need for an extra metal catalyst (details provided in the Experimental Section). As shown in Figure 1e, efficient nucleation and growth result in forming a gray Te nanomesh with uniform morphology on the polyimide (PI) substrate (Figure S3, Supporting Information). The synthesis process of the Te nanomesh is based on a multi-scale vdWs growth strategy, which is compatible with multiple substrates.[19] The formation mechanism of Te nanomesh is characterized by three consecutive processes: nucleation, lateral growth, and spontaneous self-welding, which occur sequentially throughout the vapor growth (Figure S4, Supporting Information). Due to the multi-scale vdW interactions parallel to the substrate, Te nanowires (NWs) grow laterally on the substrate and subsequently weld into nanomesh. This nanomesh morphology facilitates subsequent device integration. Notably, our nanomesh fabrication method does not involve chemical reactions, thereby preventing any associated damage to the polymeric substrates.

The SEM images in **Figure 2**a confirm the compatible growth and self-assembly of Te nanomesh on flexible PI substrates, with NW diameters of ≈150 nm and an NW density of 4.2 μm^{-2}. To investigate the correlation between the nucleation growth of Te chains and the substrate, we measured the water contact angle of both the bare PI substrate and the Te nanomesh/PI substrate (Figure S5, Supporting Information). The contact angle results indicate a lower surface energy after the growth of the nanomesh on the PI substrate. This suggests that multi-scale vdWs interactions energetically favor the energy barrier reduction for nucleation and growth, resulting in a low-energy surface for the Te nanomesh/PI substrate samples. A self-welding process is clearly observed after Te nucleation and lateral growth processes,[20] as shown in the transmission electron microscopy (TEM) image in Figure 2b. In Figure 2c, the two sets of reciprocal lattices correspond to the two welded NWs in Figure 2b, with an angle of 67.9°, which aligns well with the welding angle. The welding angles among Te NWs are random because there is no coherence or lattice epitaxy relationship between the Te NWs and the substrate.

2.2. Te Nanomesh Characterization

Various characterization methods were employed to gain further insight into the inherent properties of our Te nanomesh material. The X-ray diffraction (XRD) pattern of the Te nanomesh grown on the PI substrate is shown in Figure 2d. All characteristic peaks are consistent with the typical hexagonal crystal structure of Te (space group $P3_121$ [152]). Specifically, since the vdWs-packed Te chains grow laterally on the substrates, the [0003] diffraction peak is absent in the XRD pattern.[19,21] As depicted in the HAADF-STEM image in Figure 2e, the spiral Te chains grow along the *c*-axis of the hexagonal array. The intensity profile analysis, shown in Figure S6 (Supporting Information), reveals a plane spacing of ≈4.66 Å, corresponding to the $(\bar{1}2\bar{1}0)$ plane. Due to the distinctive helical chain structure of Te, the nonlinear optical properties of elemental Te were evaluated using second harmonic generation (SHG). As shown in Figure 2f, our material demonstrates a high-intensity and concentrated peak at ≈532 nm. This is attributed to the hexagonal crystal structure of the Te nanomesh, where the symmetry of this structure determines its nonlinear optical response.[22] A non-centrosymmetric structure can effectively generate second harmonic signals and ensure phase-matching conditions, resulting in a single strong second harmonic peak at specific wavelengths.

Furthermore, the XPS pattern of the Te 3d core levels is shown in Figure S7 (Supporting Information). The characteristic peaks at 572.3 and 582.7 eV correspond well with the Te 3d peaks.[23] Notably, no additional peaks were observed in the elemental pattern, indicating the absence of oxidized Te components on the surface. The detailed elemental composition and chemical states are presented in Figure S8 (Supporting Information). Energy dispersive spectroscopy mapping images, shown in Figure S9 (Supporting Information), further determine the elemental composition and distribution within the samples. Also, the Raman study of the Te nanomesh is illustrated in Figure 2g,i, where three first-order Raman active modes located at 89.7 cm^{-1} (E_1 mode), 118.1 cm^{-1} (A_1 mode), and 137.8 cm^{-1} (E_2 mode) were identified.[24] The E_1 and E_2 modes correspond to bond-bending and bond-stretching, respectively, while the A_1 mode represents

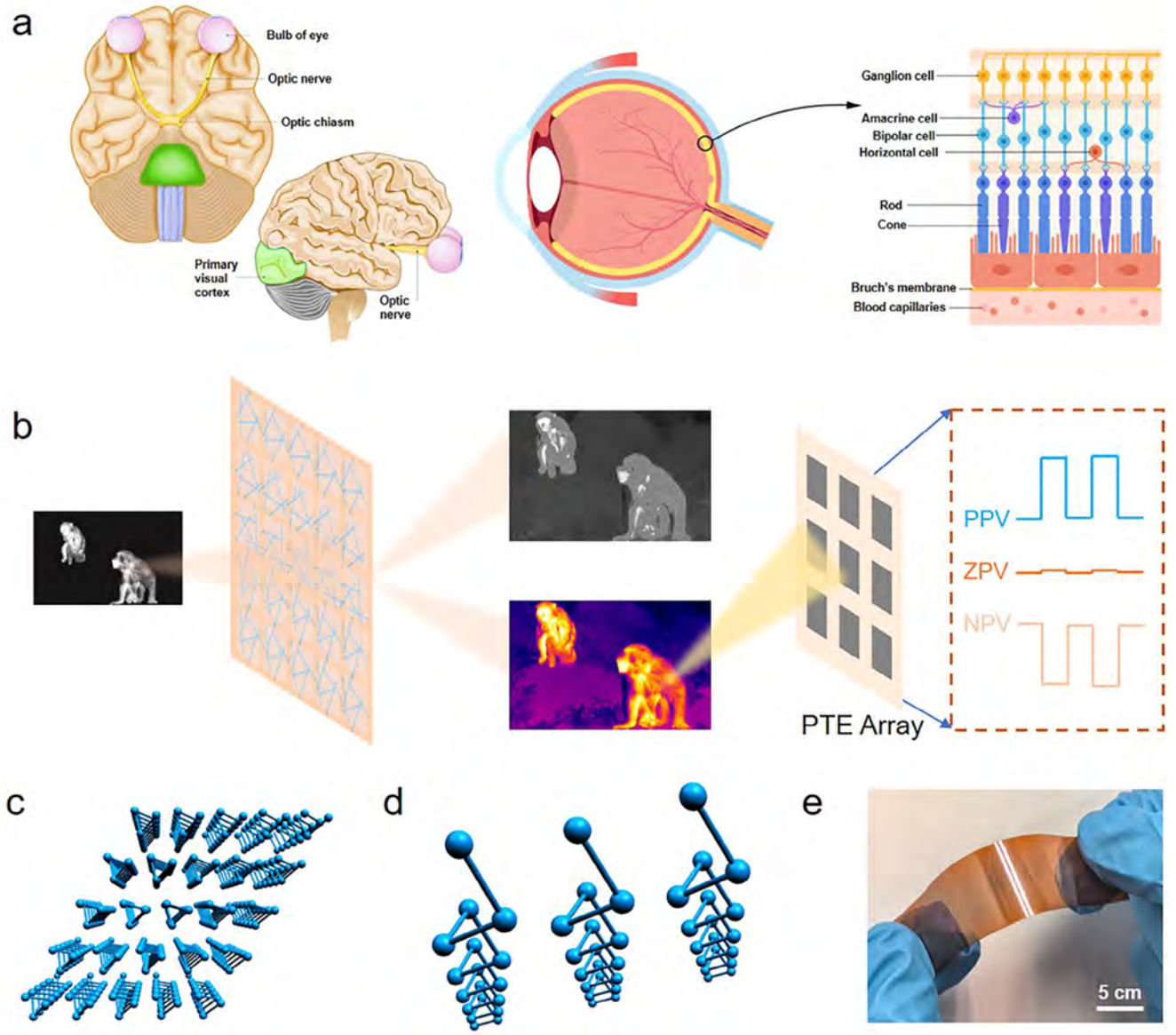

Figure 1. a) Illustration of the human visual system. The left and middle panels demonstrate the components of the human visual system. The right panel shows the detailed structure of the retina. b) The photothermal response of the flexible array based on Te nanomesh to infrared can be used for objection detection in dark conditions, generating positive and negative responses. c,d) The helical chains-like crystal structure of elemental Te. e) Te nanomesh grown on the PI substrate.

chain expansion in the basal plane. As shown in Figure S10 (Supporting Information), each mode exhibits distinct atomic vibration features, with the Te chain in the $P3_121$ space group as an example.

In this work, aiming to bypass the constraints on scalability and integrability, we use a robust vapor-phase growth method to synthesize wafer-scale Te van der Waals nanomeshes at 150 °C. This low-temperature fabrication approach avoids chemical reactions and associated damage to typical substrate materials, enabling direct growth of Te nanomeshes under atmospheric pressure, thus eliminating the need for capital-intensive equipment. It is noted that the self-assembled Te nanomesh can be grown on various surfaces, including flexible plastics, ensuring compatibility with diverse technologically functional substrates and enabling scalable, low-cost device fabrication. The Te NWs grow laterally on the substrates due to vdWs interactions parallel to the surface, forming nanomesh that align with the planar architectures of modern devices, facilitating subsequent integration. Additionally, a self-welding process during growth enhances electrical performance and mechanical robustness by creating well-connected nanomesh morphologies, reducing inter-NW junction resistance. This makes the self-welded nanomeshes a promising candidate for reliable active device components in practical applications.

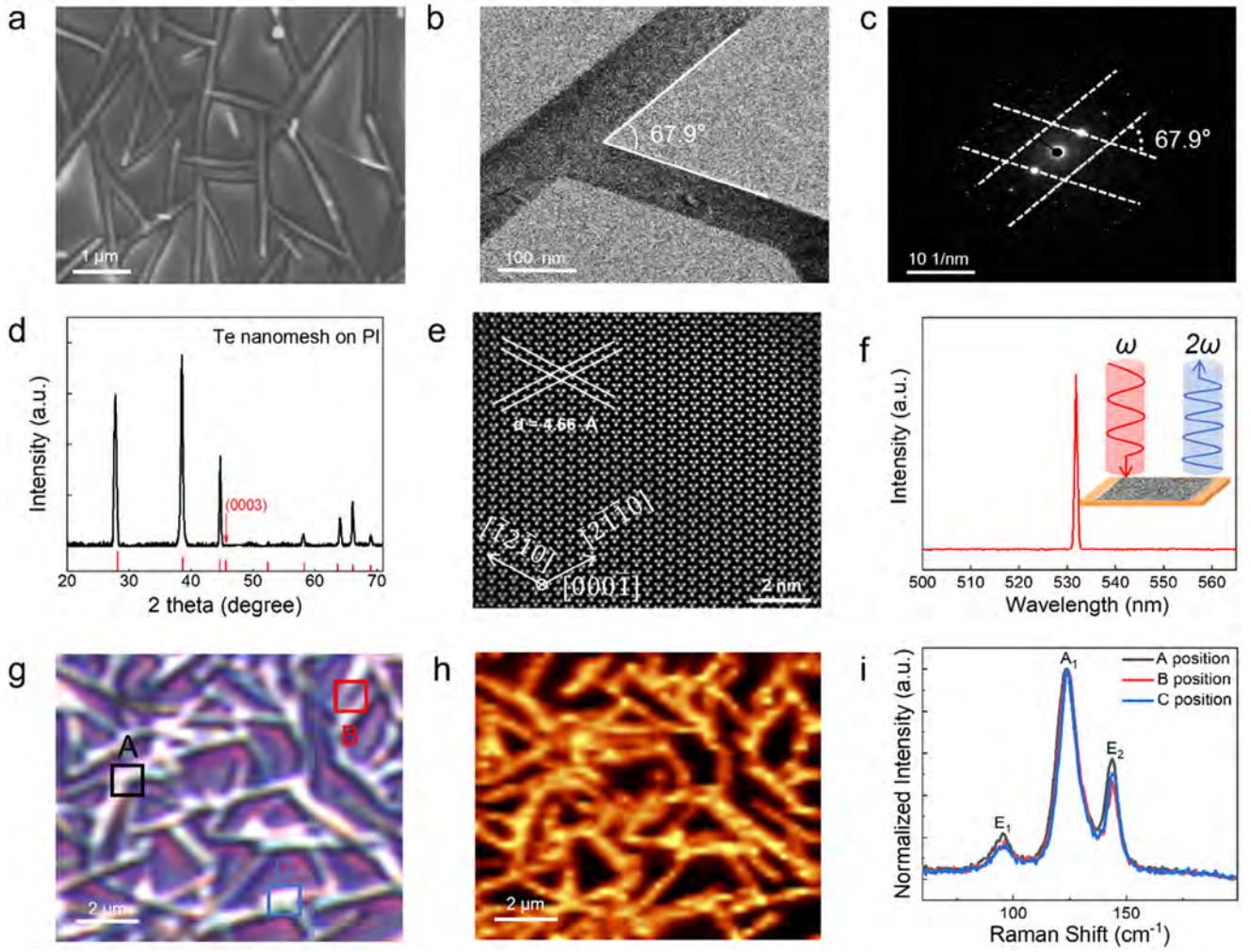

Figure 2. a) SEM image of the Te nanomesh with an NW density of 4.2 μm^{-2}. b) TEM image of the self-welding process of the Te nanomesh. c) Two groups of reciprocal lattices correspond to the two NWs in Figure 2b, indicating a specific angle between two welding NWs. d) XRD pattern of the Te nanomesh grown on the flexible PI substrate. e) High-angle annular dark field scanning transmission electron microscopy (HAADF-STEM) image of the Te NW in a cross-sectional view. f) SHG image of the elemental Te with a single peak. The left inner image is a schematic diagram of the mechanism of SHG, an incident light wave that interacts with the nonlinear medium Te nanomesh, generating a harmonic with a frequency twice the fundamental frequency. g) Microscopy image of the Te nanomesh in bright field. h) The corresponding Raman mapping and i) Raman spectra with three modes of E_1, A_1, and E_2.

2.3. PI-Based Te Nanomesh PTE Detectors

As shown in **Figure** 3a,b, the morphology of our proposed nanomesh PTE detector includes a 60 μm channel length and a nickel electrode layer. When PTE devices are irradiated by incident light, a temperature gradient is generated. The energy of the photons from the laser source is sufficient to transition through the narrow bandgap of our device, resulting in a local temperature increase. This temperature difference causes electrons and holes to migrate in response to the temperature gradients,[25,26] creating an electric field that can be observed as the output signal. Unlike traditional photoelectric detectors, our devices can modify the temperature gradient by adjusting the position of laser irradiation along the nanomesh channel, even altering or reversing the magnitude of the PTE photovoltage (Figure 3c). The scanning photovoltage mapping (SPVM) shown in Figure 3d directly exhibits an opposite photovoltage (V_{ph}) of ≈±10 mV at the two ends of the channel. Moreover, under zero bias conditions, a region near the center of the channel exists where $V_{ph} = 0$. The SPVM results indicate that Te nanomesh devices align well with typical PTE mechanisms. Based on the Seebeck effect, the V_{ph} is generated by the photo-induced temperature gradient (ΔT) as follows:

$$V_{ph} = -S \times \Delta T \quad (1)$$

where the Seebeck coefficient (S) is determined to be 356 μV K^{-1}, as shown in Figure 3e. This finding confirms that the major carrier type in the Te nanomesh is a hole, as $S > 0$ typically exists in p-type semiconductors. Our device demonstrates a stronger thermoelectric effect and better thermoelectric performance than conventional PTE counterparts like InSb, Bi_2Se_3,

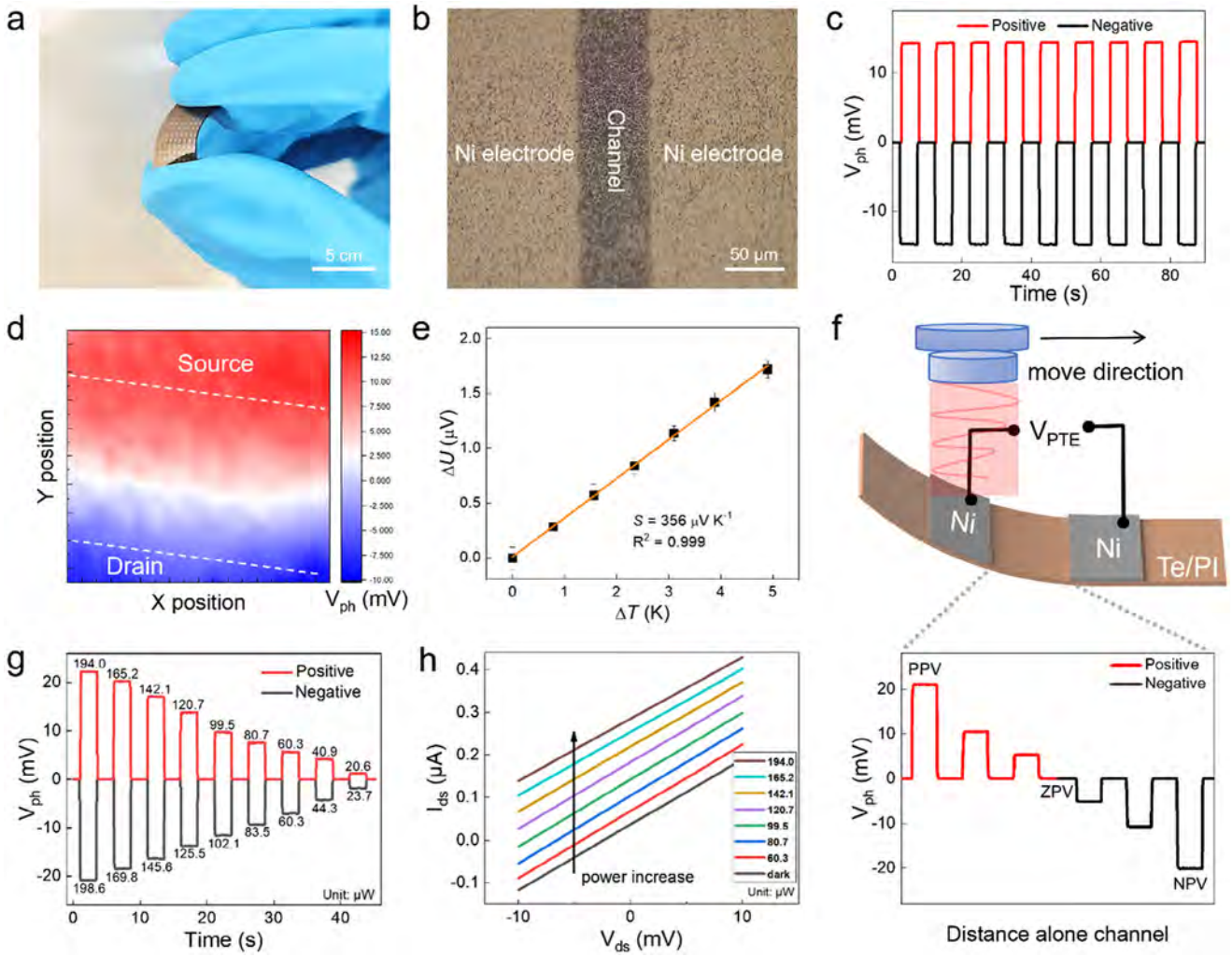

Figure 3. a) The morphology of nanomesh-based PTE devices on the flexible PI substrate. b) Optical image of the Te nanomesh device using nickel electrodes. c) Positive and negative photoresponse with laser positioning at two-channel ends. d) SPVM of nanomesh-based PTE photodetectors. e) Room-temperature Seebeck coefficient measurement of the Te nanomesh on PI. f) Schematic illustration of the local laser-induced potential distribution. g) The opposite V_{ph} curve and temporal response under increasing 1550 nm laser powers. h) *I*–*V* curves under increasing laser powers at 1550 nm.

and chalcogenide materials (see Table S1, Supporting Information). In Figure 3f, the schematic image clearly displays the local laser-induced potential distribution (ΔV) based on a PTE operation mechanism. The position-dependent modulation differs fundamentally from traditional approaches that rely on gate-tuned device states.[3,27] In contrast, the current approach of modulating light position exploits spatially localized photothermal effects, where incident photons generate position-dependent thermal gradients, driving thermoelectric voltages via the Seebeck effect.[28] The unique photoresponse behavior of the PTE detectors is shown in Figure 3g, where the maximum V_{ph} can reach 22 mV under 194 μW irradiation. Notably, according to the Seebeck coefficient, this irradiation intensity can induce a ΔT of ≈64 K. Additionally, the device output voltage increases with the 1550 nm infrared light power, and the device resistance remains steady during this process (Figure 3h).

We observed a linear relationship between the P and V_{ph} with increasing infrared light powers, as illustrated in **Figure 4a**. This linear relationship can be modeled by the power-law $V_{ph} \propto P^{\alpha}$, where the fitting factor α is close to 1, indicating that the photoresponse is thermally driven rather than by direct carrier excitation. This is in contrast to the bulk photovoltaic effect (BPVE), by which the photocurrent–power relationship of Te BPVE devices would undergo a characteristic transition from linear to sublinear dependence as the incident optical power increases.[29] Correspondingly, the responsivities ($R = V_{ph}/P$) and channel resistances remain consistent across different P values, eliminating the potential contributions of photoconductive and bolometric effects. Figure 4b,c show that the peak responsivity under 1550 nm infrared light is ≈120 V W^{-1}, surpassing most PTE detectors (Figure S11, Supporting Information). To ensure the practical application of our devices on PI, we investigated the

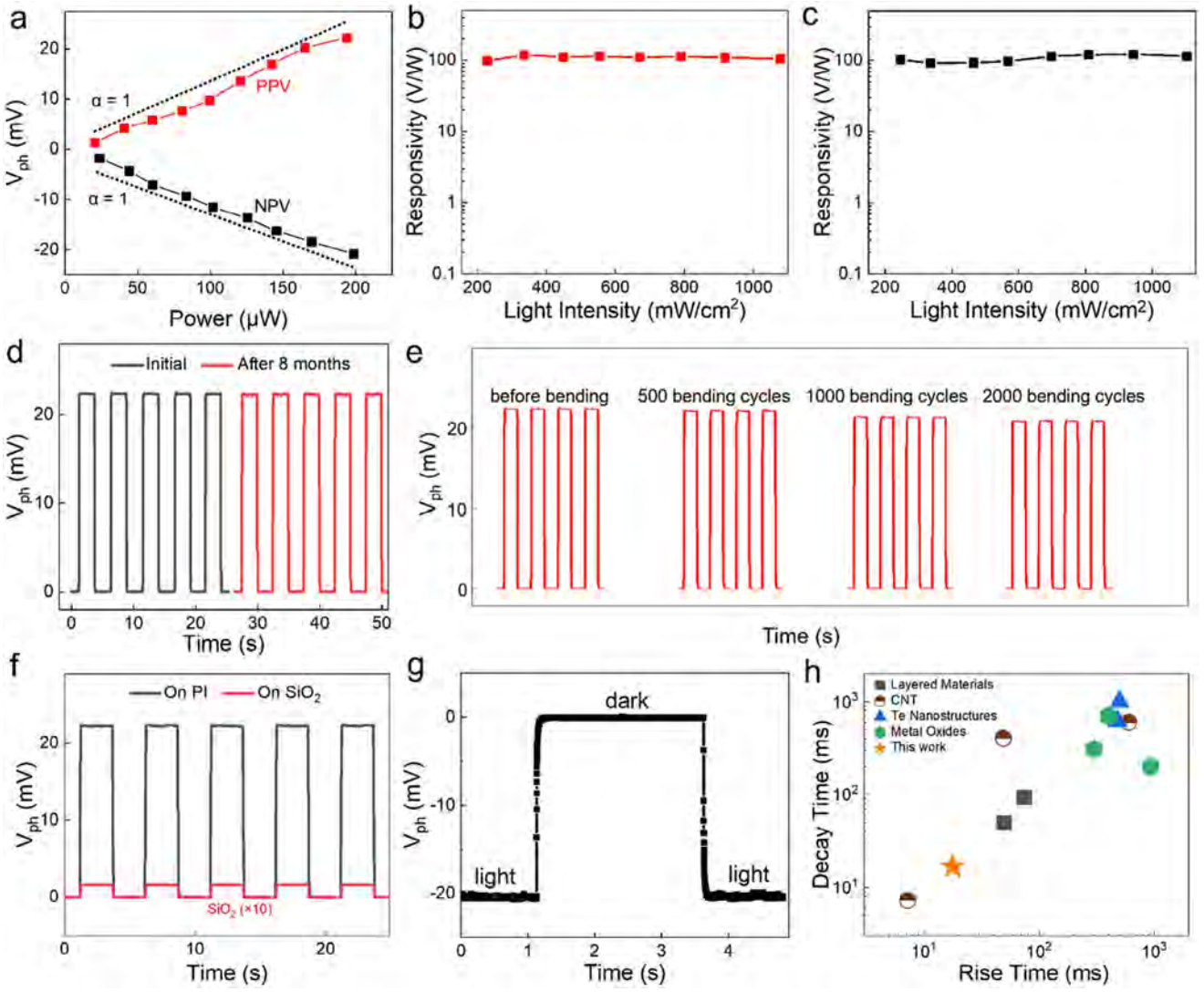

Figure 4. a) V_{ph} as a function of 1550 nm light power in PPV and NPV modes. b,c) The responsivity of positive and negative V_{ph} under different light powers. d) The environmental stability of the Te nanomesh against environmental factors after storing in ambient conditions. e) Photoresponse with varying bending cycles up to 2000 times. f) Comparison of PTE performance of the Te nanomesh on PI and SiO_2 substratesultrasonication. g) Millisecond-level response time of Te nanomesh-based PTE devices. h) Comparison of the PTE response of Te, metal oxides, carbon nanotubes, layered materials, and Te nanomesh.

environmental and bending stability of the elemental Te device. As shown in Figure 4d, after placing the sample without additional passivation in an ambient environment for 8 months, there is no evident degradation in the infrared detection performance, demonstrating its robustness against moisture and atmospheric oxygen. This result highlights that the naturally terminated vdWs surfaces of the Te nanomesh prevent surface-induced material degradation.[30] It is also noted that the devices maintain reproducible photoresponse characteristics after more than 2000 bending cycles, with less than approximately a 10% decrease in photovoltage, as shown in Figure 4e. Preferential vapor-phase condensation at the welded junctions enhances device performance by forming low-resistance ohmic-like contacts, facilitating efficient charge carrier transport. Furthermore, unlike networks fabricated via solution-phase deposition methodologies, which typically yield weak interfacial connections between NWs, our vapor-phase self-welded nanomeshes exhibit a highly integrated and continuous nanomesh architecture. This structurally optimized configuration improves mechanical integrity and demonstrates exceptional operational stability regarding repeated illumination and continuous illumination across a wide spectrum (Figures S12 and S13, Supporting Information).

To explore the impact of different substrates on elemental Te devices, we compared the photovoltages on SiO_2 and PI substrates. The results in Figure 4f indicate that the photovoltage of the device on the PI substrate (21 mV) is significantly higher than that on the SiO_2 substrate (0.2 mV). The appropriate choice of polymeric substrate can enhance the PTE effect.[31,32] Previous studies have reported that a thermal coupling effect between

substrates and Bi_2Se_3 PTE films can generate higher temperature gradients or an enhanced Seebeck coefficient, thereby improving the photovoltage and responsivity of Bi_2Se_3-based PTE detectors.[33–37]

Furthermore, the rise and decay times of the Te nanomesh were measured to be 17.9 and 16.7 ms, respectively (Figure S14, Supporting Information). Compared to other types of devices, our Te nanomesh devices do not have an advantage in response time over some CNT and layered material devices, such as Ti-CNT-Pd films. Still, they outperform most metal oxide devices by an order of magnitude (Figure 4h, Table S2, Supporting Information).[38–47] Based on the PTE mechanism, the Te nanomesh can achieve bandgap-independent detections, with responsivities under 405, 532, and 635 nm light determined to be 49.7, 28.7, and 29.1 V W^{-1}, respectively. It is noteworthy to mention that the responsivities under visible light irradiation are inferior to the infrared detection performance (Figures S9 and S15, Supporting Information). The observed decrease in responsivity under high-energy photon irradiation represents a distinct deviation from the hot electron effect. It is particular that the low-energy infrared light matches many materials' molecular vibration and rotation modes well. These modes can effectively absorb the energy of infrared light and convert it into thermal energy. Although visible light can also be absorbed by our materials and converted into thermal energy, this process is usually not as direct and efficient as the coupling between infrared light and molecular vibration modes, and the penetration depth of visible light is relatively shallow.

2.4. Convolutional Image Processing using Te Nanomesh-Based PTE Devices

By programming the illumination position to create combinations of positive photovoltage (PPV), negative photovoltage (NPV), and zero photovoltage (ZPV), the Te nanomesh-based PTE devices demonstrate potential for executing visual feature extraction. Unlike traditional hardware systems with separate detection and processing modules, the Te nanomesh-based PTE devices excel by integrating incident light with information preprocessing, thereby facilitating near-data processing. The light-induced PTE conversion process can disrupt the symmetry of the electric potential along the channel, resulting in linear photoresponsivity and a position-tunable positive and negative photoresponse, effectively implementing convolution. Given the bi-directional photoresponse of the Te nanomesh-based PTE array, we demonstrate a proof-of-principle in-sensor convolutional network for edge computing.

The input image is encoded as light intensity (P_j), and the output photovoltage follows the relation $V_{ph} = \sum R_j P_j$, with R_j representing the responsivity of each pixel. The R_j, which is tunable in both magnitude and polarity, effectively functions as the convolutional weight within a kernel matrix. A 3 × 3 Laplacian operator was implemented as a validation experiment by mapping its weights onto R_j in the array, forming a convolution kernel (**Figure 5a**). In our approach, the convolution kernel weights are directly mapped to the R_j gradient distribution of the Te nanomesh-based PTE devices, enabling an intrinsic, hardware-level implementation of edge detection. The convolution operation is performed based on the spatially varying photothermal response, where the photovoltage output is modulated by the local R_j gradient, effectively acting as a Laplacian filter. This method eliminates the need for external computation, providing a self-powered in-sensor implementation of convolution operations with enhanced efficiency, reduced noise level, and reduced power consumption (Figure S16, Supporting Information).

To ensure precise positioning of the illuminated channels relative to the image features, the device array is designed with an optimized photothermal response symmetry that closely matches the convolution kernel's gradient distribution. Furthermore, in this work, to investigate the optoelectronic characteristics of the Te nanomesh device, a customized high-precision optoelectronic scanning system was used to enable spatially resolved photoresponse analysis. With the help of a high-precision piezoelectric scanning platform, the positioning accuracy can reach μm-level in this work. This alignment allows for accurately mapping the spatial intensity variations in the input image to the corresponding photovoltage output. As illustrated in Figure 5b, the kernel was employed for edge detection, a fundamental task in image processing. When applied to thermal imaging data, the edge detection operation effectively isolated and highlighted critical spatial features, demonstrating its ability to enhance image interpretation compared to the original inputs. Building on this foundational capability, the PTE device array was further utilized to perform various image processing operations on grayscale images (Figure 5c). These operations included sharpness enhancement, reversal, and embossing, showcasing the array's adaptability for diverse image transformations. The corresponding kernel functions, their weights, and the mapping of R_j are detailed in Table S3 (Supporting Information), providing a comprehensive framework for device functionality.

The experimental results align closely with simulation outcomes, underscoring the scalability and reliability of the Te nanomesh-based PTE device array (Figure 5d). Such congruence validates the device's potential for real-world image processing applications. Furthermore, the extracted image features hold significant promise for advanced object recognition algorithms, as they enable the pre-filtering and refinement of visual data at the sensor level. By integrating simultaneous light sensing and preprocessing capabilities, the Te nanomesh-based PTE device fundamentally enhances the efficiency and speed of image-processing hardware systems. This advancement not only reduces the computational burden on downstream systems but also positions the device as a cornerstone for next-generation imaging technologies, particularly in applications requiring edge computing and real-time data processing.

3. Conclusion

In summary, we present an in-sensor convolutional network based on Te nanomesh-based PTE devices. The low-temperature lateral growth of seld-welded Te nanomesh under atmospheric pressure is governed by multi-scale vdWs interactions. We demonstrate a high Seebeck coefficient and PTE efficiency across

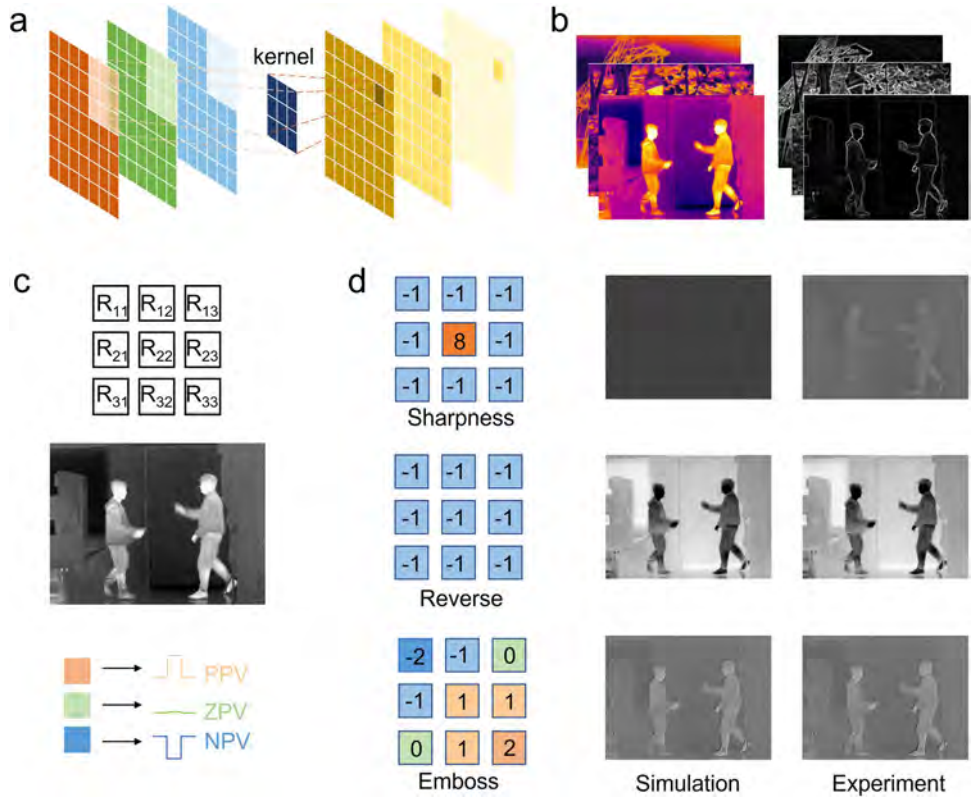

Figure 5. a) Schematic illustration of simultaneous perception and preprocessing using the PTE array as the convolutional kernel. b) Edge detection of thermal imaging data. c) Original grayscale image alongside the mapping kernel derived from the R_j of the PTE array, where orange, green, and blue correspond to the device's PPV, ZPV, and NPV states, respectively. d) Grayscale image processed using a convolutional kernel representing the selected image processing operator. Simulation results depict images processed by ideal operators, while experimental results showcase images processed by convolutional kernels mapped from R_j.

a wide spectral region by carefully designing the self-welded Te nanomesh on PI substrates. When configured into PTE detectors, these Te nanomesh devices exhibit impressive performance, with a fast response time of ≈17 ms and a high responsivity of ≈120 V W^{-1}, covering a detection range from visible light to infrared. The unique tunable photovoltage and high-symmetry bi-directional photoresponse characteristics of the photodetector array were utilized as convolutional kernels for edge computing. This work showcases the multi-scale vdWs growth of Te nanomesh on a flexible substrate, leading to superior PTE response. It offers a novel approach to convolutional image processing, enhancing both the performance and stability of PTE devices.

4. Experimental Section

Synthesis of Te Nanomesh on PI Substrates: To realize the growth process, a two-zone vapor transport system synthesized Te nanomesh on the flexible PI substrate. The analytical-grade 1 g of Te powders (Aldrich, pieces, 99.999%) was collected in a 10 mL glass test tube and positioned in the center of 1st heating zone (400–450 °C). Then, PI substrates cleaned by ultrasonication in DI water were located downstream (150–200 °C); the first piece of PI substrate was ≈15 cm from the glass test tube. Before growth, the whole system was evacuated by argon gas (Ar, 99.999%) for 20 min to remove residual oxygen. After that, Ar gas, which acted as a carrier gas, was fed into the furnace tube with a flow rate of 200 sccm. The tube chamber was regulated at 125–150 Torr pressure during growth. Eventually, after growth, the furnace tube was cooled to room temperature naturally under an Ar atmosphere, and the gray product was grown on the PI substrates.

Material Characterization: The elemental Te nanomesh crystal structures were initially analyzed by X-ray diffraction (D2 Phaser Cu Kα radiation, Bruke). In addition, the morphologies of as-prepared Te nanomesh were examined by an optical microscope (Nikon) and scanning electron microscopy (field-emission SEM, FEI Quanta 450). Raman spectra were generated by a confocal microscope spectrometer (NTEGRA Spectra system). An X-ray photoelectron spectrometer (XPS) was employed using a Thermo ESCALAB 250Xi system to evaluate the Te nanomesh materials' compositions and chemical states. Meanwhile, the water contact angles were conducted by a DataPhysics OCA 15EC Contact Angle Tester. The crystal structure was checked by TEM (CM-20, Philips) and HRTEM (JEOL 2100F). The nanomesh was transferred onto the Cu TEM grids through a polymer-assisted wet-transfer method to prepare the samples for TEM study.

Device Fabrication and Characterization: After Te nanomesh fabrication on PI, 50-nm-thick Ni electrodes with a channel length of 60 µm were deposited with a thermal evaporation rate of 1 Å s^{-1}. A semiconductor analyzer (Agilent 4155C) was employed to measure the electrical properties of Te nanomesh in a dark environment. Laser diodes of 405, 532, 635, and 1550 nm were used to act as incident light sources, while the incident power was measured by a power meter (Thorlabs PM400). An arbitrary function generator (AFG 2005) was employed to control the

light-switching operation of the laser generator. The responsivity (R) is defined as $R = V_{ph}/(P_{light} \times A)$, where V_{ph}, P_{light}, and A refer to the photovoltage, light intensity, and channel area, respectively. Photovoltage mapping was also conducted using an optoelectronic scanning system (ScanPro Advance, Metatest) to study the working mechanism of PTE detectors. In this study, the Seebeck coefficient of Te nanomesh was characterized using a thermoelectric measurement system (CTA-3, Cryoall) with an instrumental accuracy of ±5%. The measurement configuration incorporated a specialized strip-shaped thin-film sample holder (3 mm × 13 mm). A heater was utilized to establish a temperature gradient across the sample, while two thermocouples simultaneously monitored the temperature differential (ΔT) and corresponding thermoelectric voltage (ΔU) at designated measurement positions. The Seebeck coefficient (S) was subsequently determined through linear fitting analysis of the ΔU–ΔT relationship. Multiple measurements were performed on different samples to ensure reliability and statistical significance.

Convolutional Image Processing: Grayscale images were initially generated on a computer using custom scripts to simulate the required datasets for testing. The images were designed to reflect various real-world patterns and scenarios relevant to the study. In this work, two publicly available thermal infrared imaging datasets were utilized: the infrared insulator dataset and the large-scale and high-diversity general thermal infrared object tracking obtained by benchmark. The images were subjected to convolutional operations, where the high-symmetry bi-directional photoresponse characteristics of the photodetector array were utilized as convolutional kernels. The convolutional filters mapped the light responsivity characteristics onto the image, extracting key features such as edges, textures, and spatial patterns. All operations, including image manipulation and convolutional processing, were automated and controlled through Python scripts, ensuring reproducibility and consistency across the experiments.

Supporting Information

Supporting Information is available from the Wiley Online Library or from the author.

Acknowledgements

The project was supported by the Innovation and Technology Fund (Project no. MHP/126/21) from the Innovation and Technology Commission of Hong Kong SAR, China, the National Natural Science Foundation of China (Project no. 12204248), the Research Grants Council of the Hong Kong SAR, China (Project No. CRS_CityU101/24), the Science Technology and Innovation Committee of Shenzhen Municipality (Project No. JCYJ20230807114910021), Guangdong Basic and Applied Basic Research Fund (Project no. 2024A1515011922), and City University of Hong Kong (Project no. 7006109 and 7020088).

Conflict of Interest

The authors declare no conflict of interest.

Data Availability Statement

The data that support the findings of this study are available from the corresponding author upon reasonable request.

Keywords

convolutional image processing, in-sensor computing, photothermoelectric detectors, tellurium nanomesh

Received: December 14, 2024
Revised: February 24, 2025
Published online: March 4, 2025

[1] F. Liao, Z. Zhou, B. J. Kim, J. Chen, J. Wang, T. Wan, Y. Zhou, A. T. Hoang, C. Wang, J. Kang, J.-H. Ahn, Y. Chai, *Nat. Electron.* **2022**, *5*, 84.
[2] B. Ouyang, J. Wang, G. Zeng, J. Yan, Y. Zhou, X. Jiang, B. Shao, Y. Chai, *Nat. Electron.* **2024**, *7*, 705.
[3] L. Pi, P. Wang, S.-J. Liang, P. Luo, H. Wang, D. Li, Z. Li, P. Chen, X. Zhou, F. Miao, T. Zhai, *Nat. Electron.* **2022**, *5*, 248.
[4] Y. Zhu, Y. Wang, X. Pang, Y. Jiang, X. Liu, Q. Li, Z. Wang, C. Liu, W. Hu, P. Zhou, *Nat. Commun.* **2024**, *15*, 6015.
[5] X. Pang, Y. Wang, Y. Zhu, Z. Zhang, D. Xiang, X. Ge, H. Wu, Y. Jiang, Z. Liu, X. Liu, C. Liu, W. Hu, P. Zhou, *Nat. Commun.* **2024**, *15*, 1613.
[6] T. Yokota, K. Fukuda, T. Someya, *Adv. Mater.* **2021**, *33*, 2004416.
[7] Y. Yang, C. Pan, Y. Li, X. Yangdong, P. Wang, Z.-A. Li, S. Wang, W. Yu, G. Liu, B. Cheng, Z. Di, S.-J. Liang, F. Miao, *Nat. Electron.* **2024**, *7*, 225.
[8] H. Shao, Y. Ji, R. Wang, J. Liu, Y. Li, B. Liu, W. Li, Y. Xie, L. Xie, J. C. Ho, W. Huang, H. Ling, *Nano Energy* **2024**, *130*, 110133.
[9] X. Huang, Y. Liu, G. Liu, K. Liu, X. Wei, M. Zhu, W. Wen, Z. Zhao, Y. Guo, Y. Liu, *Adv. Funct. Mater.* **2022**, *33*, 2208836.
[10] M. Zhang, Z. Chi, G. Wang, Z. Fan, H. Wu, P. Yang, J. Yang, P. Yan, Z. Sun, *Adv. Mater.* **2022**, *34*, 2205679.
[11] C. Han, X. Liu, X. Han, M. He, J. Han, H. Zhang, X. Hou, H. Zhou, H. Yu, Z. Wu, J. Gou, J. Wang, *Adv. Funct. Mater.* **2022**, *32*, 2209680.
[12] H. Zheng, Y. Lu, K. H. Ye, J. Hu, S. Liu, J. Yan, Y. Ye, Y. Guo, Z. Lin, J. Cheng, Y. Cao, *Nat. Commun.* **2021**, *12*, 91.
[13] D. Kumar, H. Li, U. K. Das, A. M. Syed, N. El-Atab, *Adv. Mater.* **2023**, *35*, 2300446.
[14] T. Ahmed, M. Tahir, M. X. Low, Y. Ren, S. A. Tawfik, E. L. H. Mayes, S. Kuriakose, S. Nawaz, M. J. S. Spencer, H. Chen, M. Bhaskaran, S. Sriram, S. Walia, *Adv. Mater.* **2020**, *33*, 2004207.
[15] Z. Xie, B. Zhang, Y. Ge, Y. Zhu, G. Nie, Y. Song, C. K. Lim, H. Zhang, P. N. Prasad, *Chem. Rev.* **2022**, *122*, 1127.
[16] J. Li, X. Li, H. Zhu, *Mater. Today* **2024**, *75*, 187.
[17] X. Chen, Y. J. Park, M. Kang, S. K. Kang, J. Koo, S. M. Shinde, J. Shin, S. Jeon, G. Park, Y. Yan, M. R. MacEwan, W. Z. Ray, K. M. Lee, J. A. Rogers, J. H. Ahn, *Nat. Commun.* **2018**, *9*, 1690.
[18] S. Li, D. Ouyang, N. Zhang, Y. Zhang, A. Murthy, Y. Li, S. Liu, T. Zhai, *Adv. Mater.* **2023**, *35*, 2211855.
[19] Y. Meng, X. Li, X. Kang, W. Li, W. Wang, Z. Lai, W. Wang, Q. Quan, X. Bu, S. Yip, P. Xie, D. Chen, D. Li, F. Wang, C.-F. Yeung, C. Lan, C. Liu, L. Shen, Y. Lu, F. Chen, C.-Y. Wong, J. C. Ho, *Nat. Commun.* **2023**, *14*, 2431.
[20] S. Sen, U. M. Bhatta, V. Kumar, K. P. Muthe, S. Bhattacharya, S. K. Gupta, J. V. Yakhmi, *Cryst. Growth Des.* **2008**, *8*, 238.
[21] J.-K. Qin, P.-Y. Liao, M. Si, S. Gao, G. Qiu, J. Jian, Q. Wang, S.-Q. Zhang, S. Huang, A. Charnas, Y. Wang, M. J. Kim, W. Wu, X. Xu, H.-Y. Wang, L. Yang, Y. Khin Yap, P. D. Ye, *Nat. Electron.* **2020**, *3*, 141.
[22] L. Han, Z. Yang, Q. Yang, X. Ren, X. Zhang, B. Zhang, K. Yang, J. He, C. Li, J. Wang, *Opt. Laser Technol.* **2021**, *137*, 106817.
[23] S. Nanda, A. Bhargav, A. Manthiram, *Joule* **2020**, *4*, P1121.
[24] J. Zha, D. Dong, H. Huang, Y. Xia, J. Tong, H. Liu, H. P. Chan, J. C. Ho, C. Zhao, Y. Chai, C. Tan, *Adv. Mater.* **2024**, *36*, 2408969.
[25] N. M. Gabor, J. C. Song, Q. Ma, N. L. Nair, T. Taychatanapat, K. Watanabe, T. Taniguchi, L. S. Levitov, P. Jarillo-Herrero, *Science* **2011**, *334*, 648.
[26] M. Graham, S.-F. Shi, D. Ralph, J. Park, P. McEuen, *Nat. Phys.* **2012**, *9*, 243.
[27] X. Li, J. Wang, F. Yu, J. Chen, X. Chen, W. Lu, G. Li, *Sci. Appl.* **2025**, *14*, 47.
[28] X. Li, J. Chen, F. Yu, X. Chen, W. Lu, G. Li, *Nano Lett.* **2024**, *24*, 13255.
[29] Z. Wang, C. Tan, M. Peng, Y. Yu, F. Zhong, P. Wang, T. He, Y. Wang, Z. Zhang, R. Xie, F. Wang, S. He, P. Zhou, W. Hu, *Sci. Appl.* **2024**, *13*, 277.

[30] M. Amani, C. Tan, G. Zhang, C. Zhao, J. Bullock, X. Song, H. Kim, V. R. Shrestha, Y. Gao, K. B. Crozier, M. Scott, A. Javey, *ACS Nano* **2018**, *12*, 7253.
[31] X. Xu, J. Chen, J. Zhou, B. Li, *Adv. Mater.* **2018**, *30*, 1705544.
[32] A. I. Khan, A. Daus, R. Islam, K. M. Neilson, H. R. Lee, H.-S. P. Wong, E. Pop, *Science* **2021**, *373*, 1243.
[33] N. M. Gabor, J. C. W. Song, Q. Ma, N. L. Nair, T. Taychatanapat, K. Watanabe, T. Taniguchi, L. S. Levitov, P. Jarillo-Herrero, *Science* **2011**, *334*, 648.
[34] X. Cai, A. B. Sushkov, R. J. Suess, M. M. Jadidi, G. S. Jenkins, L. O. Nyakiti, R. L. Myers-Ward, S. Li, J. Yan, D. K. Gaskill, T. E. Murphy, H. D. Drew, M. S. Fuhrer, *Nat. Nanotechnol.* **2014**, *9*, 814.
[35] L. Viti, J. Hu, D. Coquillat, W. Knap, A. Tredicucci, A. Politano, M. S. Vitiello, *Adv. Mater.* **2015**, *27*, 5567.
[36] K. W. Mauser, S. Kim, S. Mitrovic, D. Fleischman, R. Pala, K. C. Schwab, H. A. Atwater, *Nat. Nanotechnol.* **2017**, *12*, 770.
[37] M. Badioli, A. Woessner, K.-J. Tielrooij, S. Nanot, G. Navickaite, T. Stauber, J. Garcia de Abajo, F. Koppens, *Nano Lett.* **2014**, *14*, 6374.
[38] Y. Zhang, Y. Meng, L. Wang, C. Lan, Q. Quan, W. Wang, Z. Lai, W. Wang, Y. Li, D. Yin, D. Li, P. Xie, D. Chen, Z. Yang, S. Yip, Y. Lu, C.-Y. Wong, J. C. Ho, *Nat. Commun.* **2024**, *15*, 728.
[39] M. Long, Y. Wang, P. Wang, X. Zhou, H. Xia, C. Luo, S. Huang, G. Zhang, H. Yan, Z. Fan, X. Wu, X. Chen, W. Lu, W. Hu, *ACS Nano* **2019**, *13*, 2511.
[40] B. Lv, Y. Liu, W. Wu, Y. Xie, J. Zhu, Y. Cao, W. Ma, N. Yang, W. Chu, Y. Jia, J. Wei, J. Sun, *Nat. Commun.* **2021**, *13*, 1835.
[41] X. He, X. Wang, S. Nanot, K. Cong, Q. Jiang, A. A. Kane, J. E. M. Goldsmith, R. H. Hauge, F. Léonard, J. Kono, *ACS Nano* **2013**, *7*, 7271.
[42] Y. Liu, Q. Hu, Y. Cao, P. Wang, J. Wei, W. Wu, J. Wang, F. Huang, J. L. Sun, *ACS Appl. Mater. Interfaces* **2022**, *14*, 29077.
[43] R. Wang, Z. He, J.-L. Wang, J.-Y. Liu, J.-W. Liu, S.-H. Yu, *Nano Lett.* **2022**, *22*, 5929.
[44] X. Zhang, J. Jiang, A. A. Suleiman, B. Jin, X. Hu, X. Zhou, T. Zhai, *Adv. Funct. Mater.* **2019**, *29*, 1906585.
[45] F. Li, Y. Meng, R. Dong, S. Yip, C. Lan, X. Kang, F. Wang, K. S. Chan, J. C. Ho, *ACS Nano* **2019**, *13*, 12042.
[46] Y. Wang, P. Wang, Y. Zhu, J. Gao, F. Gong, Q. Li, R. Xie, F. Wu, D. Wang, J. Yang, Z. Fan, X. Wang, W. Hu, *Appl. Phys. Lett.* **2019**, *114*, 011103.
[47] P.-H. Huang, Y.-C. Shen, C.-Y. Tung, C.-Y. Huang, C. S. Tan, R.-H. Horng, *ACS Appl. Electron. Mater.* **2020**, *2*, 3515.